Precise definition of a 'Monolayer Point' in covalently attached polymer films for defining highly coherent inorganic thin films by Vapor Phase Infiltration

R. Lundy^, P. Yadav^, N. Prochukhan^, E. Giraud^, T. O'Mahony^, A. Selkirk^, E. Mullen^, J. Conway*, M.M. Turner*, S. Daniels*, P.G. Mani-Gonzalez$, M. Snelgrove~, J. Bogan~, C. McFeely~, R. O'Connor~, **E. McGlynn**~,*, G. Hughes~,*, C. Cummins^, M.A. Morris^

~School of Physical Sciences, Dublin City University, Glasnevin, Dublin 9, Ireland

*National Centre for Plasma Science and Technology

^AMBER Research Centre and School of Chemistry, Trinity College Dublin, Dublin, Ireland

$Institute of Engineering and Technology, Department of Physics and Mathematics, Autonomous University of Ciudad Juárez, Cd. Juárez 32310, Mexico

ABSTRACT: We describe a versatile bottom-up approach to covalently and rapidly graft hydroxyl terminated poly (2-vinyl pyridine) (P2VP-OH) polymers in 60 seconds that can subsequently be used to fabricate high quality TiO_2 films on silicon substrates. A facile strategy based upon room temperature titanium vapor phase infiltration of the grafted P2VP-OH polymer brushes produces TiO_2 nanofilms of 2-4 nm thickness. In order to fabricate coherent inorganic films with precise thickness control, it is critical to generate a high-quality polymer brush film i.e. a complete monolayer. Definition of precise and regular polymer monolayers is straightforwardly achieved for polymers which are weakly interacting with one another and the substrate (apart from the reactive terminal group used for grafting). However this is much more challenging for reactive systems. Crucial parameters are explored including molecular weight and solution concentration for grafting dense P2VP-OH monolayers from the liquid phase with very high coverage and uniformity across wafer scale areas. Additionally, we compare the P2VP-OH polymer system with another reactive polymer PMMA-OH and a relatively non-reactive polymer PS-OH, the latter we prove to be extremely effective for surface blocking and deactivation. Our methodology provides new insight into the grafting of polymer brushes and their ability to form dense TiO_2 films. We believe the results described herein are important for further expanding the use of reactive and unreactive polymers for fields including area selective deposition, solar cell absorber layers and antimicrobial surface coatings.

INTRODUCTION

Continued miniaturization of semiconductor devices has led to cost and integration issues [1] and challenge the manufacture of a 3 nm node as envisaged by the Samsung and TSMC foundries for 2023 [2,3]. Gate voltage scaling at these dimensions necessitates state-of-the-art architectures beyond FinFETs such as gate-all-around FET technology, leading to further integration complexity [4]. Approaches complimenting photolithography include nanoimprint lithography [5,6], block copolymer lithography [7–14] and, recently, area selective deposition (ASD) [15–17]. Such methods are favorable in enabling future device integration and help alleviate fabrication demands, e.g. litho-etch-litho-etch. The ability of ASD to selectively include many materials sets such as oxides, dielectrics and metals provides a simple route to produce material patterns and reduce the number of processing steps. The capacity of ASD to produce uniform metal and oxide layers can assist development of silicon device technologies [18] and the techniques discussed herein can have considerable importance due to the low process temperature (<500 °C) needed for CMOS fabrication [19]. ASD is promising for implementation and cost reduction in fields beyond CMOS processing, where stacked or patterned layers are required e.g. energy harvesting surfaces [20] and advances in catalysis [21]. ASD has even been demonstrated for fabricating Pt electrodes within solid oxide fuel cells [22].

Various innovative ASD approaches have been reported, typically focusing on self-assembled monolayers (SAMs) or unreactive polymeric resist layers combined with atomic layer deposition (ALD) of metal and dielectric films. For instance, Leskelä et al. designed an approach using patterned SAMs to generate features on copper and silicon substrates [23–25] as well as patterned organic films for activation [26,27] and deactivation [28,29] layers for multiple ALD processes. SAMs have been used by Bent et al. to mask and pattern copper lines on silicon [30,31] and several other substrate materials [32–36] followed by ALD metallization. Further, the Bent group has demonstrated a process for topographic selective anisotropic deposition of platinum via ALD by deactivating horizontal regions with (ion implanted) fluorocarbons [37].

Kessels et al. have incorporated area selective ALD approaches that use organic inhibitors with ALD precursors [38], surface activation via reactive plasma micro patterning [39] and tuning the oxygen ALD cycle exposure to selectively nucleate platinum on wafer regions [40]. The research extends to area-selective ALD on graphene surfaces (resist free) [41] and ASD of ZnO by area activation using electron beam-induced deposition [42]. Mackus et al. utilized several ASD approaches combined with ALD. These involved catalytic oxygen activation of noble metal surfaces [43], using a triple step ALD cycle with a selective organic inhibitor, precursor and reactive plasma [44]. The group also demonstrated selective deposition of ruthenium on Pt/SiO_2 line space using ALD and atomic layer etching (ALE) cycles [45]. Parsons et al. demonstrated selective deposition of materials (Ru, TiN, TiO_2 and HfO_2) via ALD on silicon nitride and silicon substrates by deactivating wafer areas with SAMs [46], using patterned amorphous carbon [47] and by exploiting inherent substrate selectivity [48–50]. The group also developed a TiO_2 ASD approach using ALD/ALE cycles [51]. Bates et al. introduced precise design rules for an area selective technique known as 'spin dewetting' that exploits modification of surface energies of line-space patterns [52,53]. Selectivity is induced by tuning polymer design to promote preferential dewetting from one substrate material and uniform wetting on the other.

Our previous work demonstrated the feasibility of using polymer brush (note that a brush in this sense is a film of polymer which is covalently attached to the film surface through a reactive terminal group) films to selectively deactivate patterned Cu/SiO_2 line space for ASD of metal layers [54]. The brush was selectively grafted using end groups that bind to site-specific wafer regions. Further, we demonstrated a simple approach for rapid grafting (in seconds) of end functionalized reactive polymer brush films with complete coverage and subsequent conversion to various oxides (Al_2O_3 [55], Co_3O_4 [56], CuO [57,58]) via liquid phase metal ion insertion. Surface deactivation was also achieved using a PS-OH brush that prevents the deposition of ions.

Liquid phase deposition of metal ions on grafted brushes has many benefits due to the multitude of readily available, low cost and easily prepared (water soluble) salt precursors. However, developing a vapor phase brush infiltration approach can be beneficial for a wide array of applications (both ASD and blanket layers), due to its simple one-step inclusion method, industry ready integration and very low processing temperature. A vapor phase inclusion technique can deposit uniform ultra-thin films compared to relatively high temperature routes such as CVD and PVD. Evaporation and CVD-based techniques cannot achieve high-quality 2D nano films with precise thickness control over large areas [59]. Titanium is an attractive model species for vapor phase brush infiltration given its use in a variety of far reaching applications *e.g.* TiO_2 films are routinely fabricated by sol-gel [60], pulsed laser deposition [61], chemical vapor deposition [62] and ALD [63,64]. TiO_2 coatings are widely used in self-cleaning technologies [65], as an electrode support [66], as a dielectric medium [67], and in photocatalysis [68]. ALD grown TiO_2 nanofilms have been used in many applications: corrosion protection layers on copper [69], in high-κ dielectrics, solar cells (perovskite) [70], carbon nanotubes [71] and composite nanostructures for water splitting to name a few [72].

In this article, a proof-of-concept technique for vapor phase infiltration of covalently grafted polymer brushes to produce wafer-scale TiO_2 with high uniformity is demonstrated on Si substrates. To fabricate coherent inorganic films with precise thickness control, it is critical to generate high-quality polymer brush films i.e. a complete monolayer. Definition of a polymer monolayer with complete coverage can be achieved and is straightforward for weakly interacting films but is considerably more challenging for reactive systems. We chose poly-2-vinyl pyridine, hydroxy-terminated (P2VP-OH) (Figure 1 (a)) due to the strong metal-pyridine binding interactions observed for a myriad of metal ions including Ti [73,74]. The crucial parameters necessary for grafting P2VP monolayers from the liquid phase with very high coverage and uniformity are explored. Factors such as polymer molecular weight (4 - 16 kg mol^{-1}), concentration of casting solution (0.01 – 6 wt. %) and quantity of end groups (mono/di hydroxy terminated) are examined (Table 1). We compare grafting parameters to another reactive polymer PMMA-OH (Figure 1 (b)) and a relatively non-reactive polymer PS-OH (Figure 1 (c)). The high-quality grafted P2VP brushes were exposed to vapor phase titanium tetraisopropoxide (TTIP) (Figure 1 (d)). Conversion to TiO_2 is performed using UV/ozone processing. Control over the final oxide thickness (≈ 2-4 nm) is demonstrated by adjusting the polymer molecular weight. This organometallic precursor (and component of the Sharpless epoxidation) was chosen for its ability to selectively deposit Ti^{4+} cations within the hydrophilic domains of self-assembled block copolymers in our previous work [75]. Finally, the potential of a PS brush for substrate deactivation by limiting TTIP infiltration is highlighted. The fundamental insights obtained herein can illuminate ways to utilize polymer brush films for vapor phase film and ASD device-fabrication strategies.

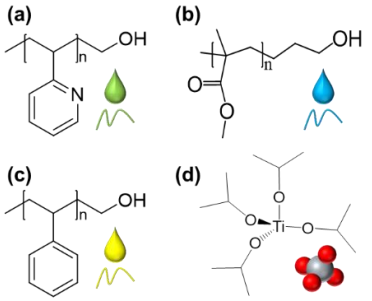

Figure 1. Hydroxy-terminated **(a)** Poly-2-vinyl pyridine **(b)** Poly(methyl methacrylate) and **(c)** Polystyrene. **(d)** Titanium tetraisopropoxide.

Table 1 – Polymer properties and annealing conditions

Polymer	Mn (kg/mol)	End group (-OH)	Anneal Conditions
P2VP-OH	4.0	mono/di	60 s (230 °C)
	6.2	mono	60 s (230 °C)
	10.0	mono	60 s (230 °C)

	16.0	mono	60 s (230 °C)
PS-OH	6.0	mono	60 s (150 °C)
	10.0	mono	60 s (150 °C)
	16.0	mono	60 s (150 °C)
PMMA-OH	6.3	mono	90 s (190 °C)

EXPERIMENTAL SECTION

Materials. Functionalized polymers: Poly-2-vinyl pyridine, hydroxy-terminated (P2VP-OH): 4 kg mol^{-1} (P18796-2VPOH) (PDI: 1.06), 6.2 kg mol^{-1} (P7544-2VPOH) (PDI: 1.05), 9.6 kg mol^{-1} (P19125-2VPOH) (PDI: 1.07), 16 kg mol^{-1} (P19128-2VPOH) (PDI: 1.11), di-hydroxy-terminated P2VP: 4 kg mol^{-1} (P18798-2VPOH) (PDI: 1.06). Poly(methyl methacrylate), hydroxy-terminated (PMMA-OH): 6.3 kg mol^{-1} (P1763-MMAOH) (PDI: 1.06). Polystyrene, hydroxy-terminated (PS-OH): 6 kg mol^{-1} (P11116-SOH) (PDI: 1.05), 10 kg mol^{-1} (P18787-SOH) (PDI: 1.09), 16 kg mol^{-1} (P13135-SOH) (PDI: 1.09). The polymers have glass transition temperatures of T_g = 95 °C, 91 °C and 85 °C for PS-OH, P2VP-OH and PMMA-OH respectively.

Homopolymers: Poly-2-vinyl pyridine (P41306-2VP) (PDI: 1.04), Polystyrene (P9405-S) (PDI: 1.03). All polymers were purchased from Polymer Source (Canada) and used without further purification.

Solvents: Tetrahydrofuran (THF) (inhibitor free), toluene, (MERCK, Ireland) were high-performance liquid chromatography (HPLC) grade and used as received. Deionized water (ρ = 18.2 MΩ.cm) was used were necessary.

Precursor: Titanium tetraisopropoxide (TTIP) (99.999%) (MERCK, Ireland) was used as received.

Pure P2VP, PS ,PMMA and SiO_2 Reference Substrates. Unfunctionalized P2VP, PS and PMMA homopolymers were used to fabricate reference substrates. The powders were each dry-pressed into disc-shaped pellets (≈ 2 mm thick) at 350 MPa in a 13 mm diameter steel pellet die (Specac, 13 mm evacuable pellet die). The pellets were exposed to solvent vapors (THF for P2VP and toluene for PS and PMMA) until a smooth mirror like surface was produced, similar to our previous work [55]. These substrates are used to determine the baseline contact angles for pure polymer surfaces to infer brush coverage on Si substrates. Plasma cleaned SiO_2 was used as a reference.

Polymer Brush Grafting. Silicon substrates (with native oxide) were cleaned and hydroxyl functionalized using an oxygen plasma treatment for 60 s (40 kHz, 50 W, Barrel Asher). P2VP-OH was dissolved in THF, PMMA-OH and PS-OH were dissolved in toluene by stirring overnight at room temperature. Polymer-solvent casting solutions were prepared at concentrations from 0.01 – 6 wt. % and spin coated at 3000 rpm for 30 s. Samples were placed on a hotplate and annealed at: 150 °C for 60 s (PS-OH), 190 °C for 90 s (PMMA-OH) and 230 °C for 60 s (P2VP-OH) for covalent grafting on SiO_2 via condensation reactions [76,77]. See Figure S1 for TGA analysis showing max process temperatures for each polymer. Following this samples were sonicated in respective solvents for 20 min (2 x 10 min washes) to remove physisorbed, ungrafted polymer material.

Titanium Dioxide Fabrication. For the TTIP infiltration process, grafted monolayer films of 0.2 wt. % P2VP (4 and 6 kg mol^{-1}) and 0.2 wt. % PS were used (6 kg mol^{-1}). Samples were place upside-down in a sealed glass chamber (height: 50 mm, diameter: 24 mm) containing ≈ 1 ml TTIP for 2 hr. at 20 °C (partial pressure ≈ 53 Pa) [78]. Polymer ashing and conversion to titanium dioxide was achieved by UV/ozone exposure (3 hr.) (Novascan PDSP-UV4).

Characterization. Field emission scanning electron microscopy (FESEM, Carl Zeiss Ultra) was performed using a secondary electron detector (InLens) with an accelerating voltage 1 - 2 kV. Focused ion beam etching (FIB, Helios Nanolab 460) was used for preparing lamella specimen using standard high kV milling and a low kV final polish, this rendered the lamella electron transparent indicating an appropriate thickness for TEM. A capping layer of e-beam platinum (~ 100 nm) and ion-beam Pt (~2 micron) was used for FIB lamella. Transmission electron microscopy (TEM, FEI Osiris) was performed using brightfield and STEM imaging. During STEM detector lengths were 220, 550 and 770 mm. The accelerating voltage was 200 kV. The EDX beam current was 1 nA, acquisition time: 30 min. Atomic force microscopy (AFM, Park Systems XE7) was used with a non-contact cantilever (AC160TS, force constant ≈26 Nm^{-1}, resonant frequency ≈ 300 kHz).

X-ray photoelectron spectroscopy (XPS, VG Scientific ESCAlab Mk II) was performed under ultra-high vacuum conditions (<5 x 10^{-10} mbar) using a hemispherical analyzer and Al Kα X-rays (1486.6 eV). The emitted photoelectrons were collected at a take-off angle of 90 ° from the samples surface. The analyzer pass energy was set to 100 eV for survey scans and 20 – 40 eV for high-resolution core scans, yielding an overall resolution of 1.5 eV. Photoemission peak positions were corrected to C 1s at a binding energy of 284.8 eV.

Dynamic contact angle (CA) measurments (custom built system) were recorded on five different regions of each sample using a high-speed camera (60 Hz sampling rate) to capture the advancing and receding CAs of three probe liquids (water, diiodomethane and glycerol). Liquids were dispensed with flow rates of 5 nls^{-1} using a 35-gauge needle (Ø135 μm OD) with droplet volumes between 40-100 nl. Surface energy analysis was determined from the advancing CAs of the three probe liquids using the Lifshitz-van der Waals/acid-base approach [79].

Dynamic Light Scattering (DLS, Malvern Zetasizer Nano ZSP) was performed on the polymer casting solutions.

Thermogravimetric analysis (TGA, Pyris 1) was performed on the functionalized polymers at a temperature range of 25°C - 700°C for 90 min.

RESULTS AND DISCUSSION

Monolayer Point of a Grafted Polymer Brush. The Hansen approach was used to identify selective polymer-solvent casting solutions (P2VP/THF and PS/toluene respectively) and is described in detail elsewhere [55]. Figure 2 shows examples of the 6 kg mol^{-1} P2VP-OH grafted from so-

lutions of solvents above and below the critical agglomeration concentration (CAC) to silicon substrates. The SEM image in Figure 2 (a) is characteristic of a well grafted brush monolayer, cast from a 0.2 wt. % solution. See Figure S2 for higher magnification SEM images. The TEM image in Figure 2a (inset) shows the brush film has high uniformity and a thickness ≈ 4 nm (see Figure S3 for TEM of the 4 kg mol^{-1} grafted monolayer ≈ 3.4 nm). By contrast the SEM image in Figure 2 (b) cast from a 2.0 wt. % solution is an example of a poorly grafted film of 6 kg mol^{-1}. Polymer coverage is uneven and shown in more detail in Figure S4. The nature of P2VP-OH material displayed in Figure 2 (b) suggests that ideal conditions are not satisfied to define the observed structure as a brush film.

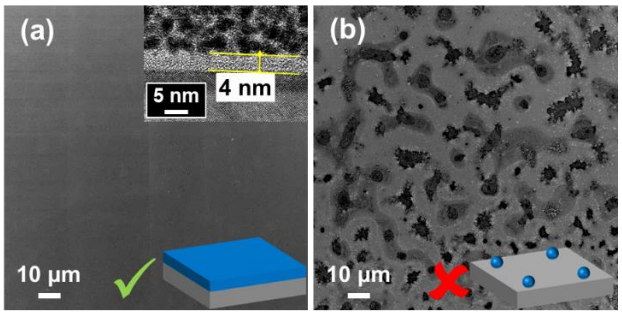

Figure 2. SEM image of a grafted P2VP-OH (Mn = 6 kg mol^{-1}) cast **(a)** below the CAC (with TEM image in inset) showing a uniform monolayer and **(b)** above the CAC with uneven coverage.

Di-hydroxy terminated 4 kg mol^{-1} P2VP was end-grafted but uniform monolayer coverage was unsuccessful even at very low concentrations (< 0.1 wt. %) (see Figure S5 (a)). Large agglomerations are present throughout the film, consistent with hydroxy end groups grafting to adjacent polymer end groups during annealing. We also note that P2VP-OH polymer with molecular weights of 10 and 16 kg mol^{-1} did not form uniform monolayers (Figure S5 (b) and (c)). DLS studies were performed on the casting solutions to elucidate the impact of concentration and molecular weight on the grafting mechanism. DLS of P2VP-OH (Mn = 6 kg mol^{-1}) casting solutions shown in Figure 2 (0.2 wt. % vs 2.0 wt. %) show an increase in agglomeration size with concentration (Figure S6 (a) and (b)). Figure S6 (c) shows an increase in agglomeration size with molecular weight at fixed concentration (0.2 wt. %). The increase in agglomeration size in the casting solutions with concentration or molecular weight is consistent with the particularly strong pyridine-pyridine stacking interactions of the P2VP molecular system [80]. Figure 3 displays a schematic of the proposed grafting mechanism above and below the CAC. As the casting solution concentration or polymer molecular weight increases, larger sized agglomerations deposit on the substrate following spin-coating. Above the CAC the agglomerates are sufficiently large that steric repulsion effects begin to prevent formation of a uniform coating *i.e.* gaps develop between agglomerates. Upon annealing, the chains near the substrate reptate and successfully locate the surface to overcome the thermodynamic reaction barrier to condensation. The physisorbed overlayers are removed during the solvent wash to reveal an uneven coating. Below the CAC, a uniform brush monolayer can be prepared for TTIP vapor infiltration.

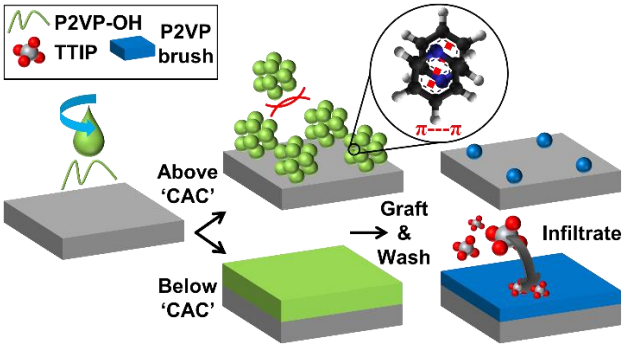

Figure 3. Schematic representation of the grafting process above and below the CAC for P2VP-OH (molecular weight: 6 kg mol^{-1}). Poor coverage occurs above CAC due to strong pyridine-pyridine stacking interactions. The P2VP monolayer brush can be infiltrated with TTIP and converted to TiO_2 using UV/ozone.

Figure 4 shows optimization data used to determine the monolayer point for grafting 4 and 6 kg mol^{-1} P2VP-OH to silicon substrates. Solutions (0.01 – 6 wt. %) were cast, grafted via baking and advancing water contact angle (WCA) measurements were immediately recorded, shown in Figure 4 (a). The control reference SiO_2 sample has an average advancing WCA of θ_{SiO2} = 4.0° ± 0.4°. At 0.01 wt. %, the average advancing WCA increases to $\theta_{P2VP(\mathbf{4k})}$ = 47.4° ± 0.8° and $\theta_{P2VP(\mathbf{6k})}$ = 57.1° ± 2.6° respectively. Above 0.05 wt. %, the advancing WCAs rapidly asymptote and saturate with an average advancing WCA of $\theta_a \approx$ 77°, similar to the value obtained for the pressed P2VP pellet ($\theta_{P2VP(max)}$ = 76.7° ± 1.6°). This trend holds for the 4 kg mol^{-1} polymer, however above a concentration of ≈ 1 wt. % the 6 kg mol^{-1} P2VP-OH rapidly transitions to a highly wetting surface ($\theta_{P2VP(\mathbf{6k})}$ < 10°) consistent with very low grafting density.

The observed θ_a behavior of the P2VP-OH brush surfaces is correlated to surface coverage using the Cassie-Baxter equation [81,82] with the assumption of surface energy heterogeneity at the molecular scale [83],

$$\Phi = \left(\frac{\cos\theta_{conc}}{\cos\theta_{SiO2}} - 1\right) \Big/ \left(\frac{\cos\theta_{P2VP(max)}}{\cos\theta_{SiO2}} - 1\right), (\mathbf{1})$$

where Φ is the apparent surface coverage of the grafted polymer brush, θ_{conc} is θ_a measured at a given grafting concentration and $\theta_{P2VP(max)}$ is θ_a of the pure P2VP pellet. Figure 4 (b) shows the change of surface coverage with solution concentration for the brush samples, calculated from equation 1. The increased Φ at the low dilution limit (0.01 wt. %) for the 6 kg mol^{-1} vs 4 kg mol^{-1} P2VP-OH brush is consistent with a longer chain length *i.e.* more surface coverage for equivalent condensation reactions. Additionally, we used X-

ray photoelectron spectroscopy in order to provide further confirmation of the grafting behavior of the 4 kg mol^{-1} and 6 kg mol^{-1} P2VP-OH systems. The N *1s* signal (~ 401 eV) from grafted brushes was tracked over the concentration range in Figure 4 (c). A strikingly similar evolution profile to Figure 4 (a) and (b) is observed from the XPS N *1s* data, consistent with the coverage level determined by WCA and Cassie-Baxter equation. Figure 4 (d) – (f) are AFM images of the 4 kg mol^{-1} P2VP-OH grafted brush (0.2 wt. %, 2.0 wt. %, 6.0 wt. %). The films are very smooth with high coverage, RMS roughness ≈ 0.6 nm (average of 3 AFM scans). The roughness factor r, defined as the ratio of actual surface area to projected area, was calculated from the height images < 1.04, representing minimal contribution to surface wettability as per the Wenzel equation, $\cos\theta_{apparent} = r\cos\theta$ [84]. For the 6 kg mol^{-1} brush (Figure 4 (g) – (i)) only the 0.2 wt. % shows good uniformity and coverage. See figure S7 for detailed surface energy analysis of the grafted brushes. At high coverage the dispersive and polar components match that of the pure polymer pellet, and the silicon control at low coverage (figure S7 (a)). The same trend is observed for the Lewis acid and Lewis base interactions (figure S7 (b))

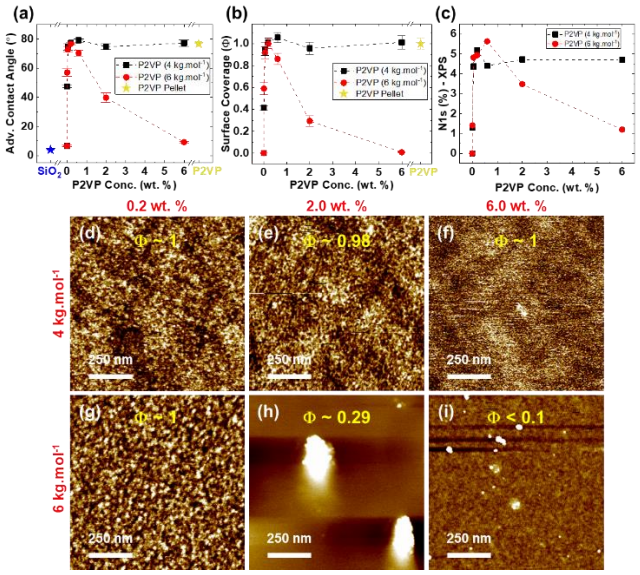

Figure 4. (a) Advancing WCAs of the 4 and 6 kg mol^{-1} P2VP brush samples grafted on silicon substrates over a range of concentrations with corresponding coverage **(c)**. **(d)** XPS nitrogen (N 1s) atomic percentage of the grafted polymers as a function of concentration. AFM topographic images of the P2VP brushes grafted from 0.2 – 6 wt. % solutions for **(d)** - **(f)** 4 kg mol^{-1} and **(g)** - **(h)** 6 kg mol^{-1} P2VP-OH.

The grafting process was tested with PS-OH (Mn = 6.0 – 16.0), as shown in Section S2. Grafting high quality uniform monolayers was achievable at all molecular weights and concentrations (> 0.01 wt. %). PMMA-OH (Mn = 6.3) was tested (Section S3) with high-quality monolayers observed even for 6.0 wt. % grafting solutions. These less reactive brushes can graft monolayers at higher molecular weight and concentration compared with PVP where stronger intermolecular forces exist between the molecules due to substantial π-orbital interactions [80]. Casting at elevated temperature, or using a more selective solvent, is also a possible route to high molecular weight PVP based monolayer films.

Polymer Brush Exposure/Infiltration to Titanium Isopropoxide. The optimized 4 and 6 kg mol^{-1} P2VP-OH brush monolayers were exposed to TTIP vapors and converted to TiO_2 films (see experimental for TTIP infiltration conditions). The Ti 2p XPS spectra in Figure 5 (a) shows the TTIP infiltrated brushes and its conversion to TiO_2. Both brushes were treated in the same TTIP processing conditions, however ≈ 50 % more precursor uptake is measured in the 6 kg mol^{-1} brush. TiO_2 is formed after UV/Ozone exposure with the Ti $2p_{3/2}$ and Ti $2p_{1/2}$ peaks at ≈ 458 and 464 eV respectively [85]. A slight reduction in the Ti signal occurs following ashing due to partial removal of TTIP precursor. The O 1s spectra in Figure 5 (b) displays the TTIP infiltrated P2VP-OH brush (Mn = 6.2) before and after UV/ozone exposure. Before UV/ozone, the Ti^{4+}, SiO_2 and isopropoxide peaks are observed at ≈ 529.7 eV (Ti-O bonds), ≈ 531.7 eV and ≈ 532.5 eV (C-O bonds) respectively [75,85]. Post UV/ozone, we observe the absence of the isopropoxide peak and partial loss of the Ti^{4+} peak is observed. There is an increase in the SiO_2 peak due to reduced attenuation of the substrate signal. Before UV/ozone, the N 1s region (Figure 5 (c) has a peak at ≈ 399 eV associated with C=N-C pyridine bonds [86,87] while after UV/ozone, the pyridine signal is absent (within XPS detection limits) indicating total removal/conversion of brush material. See Figure S15 for the survey spectra.

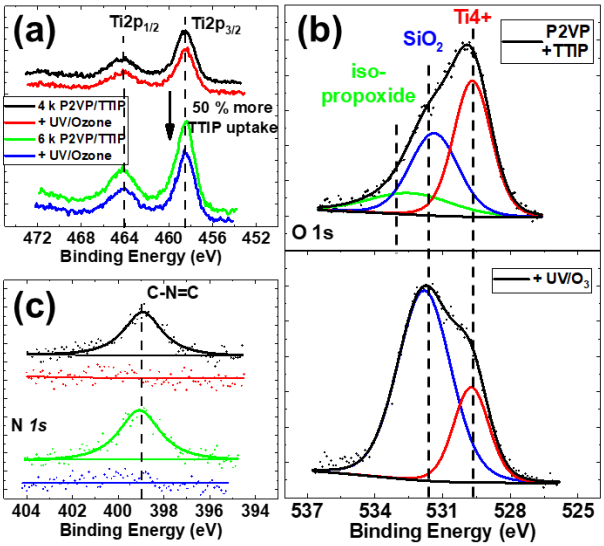

Figure 5. XPS high-res spectra of grafted 4 and 6 kg mol^{-1} P2VP-OH brushes exposed to TTIP and following uv/ozone for **(a)** Titanium 2p **(b)** Oxygen 1s and **(c)** Nitrogen 1s.

The TEM image in Figure 6 (a) is of a TiO_2 film (≈ 4 nm thick) produced using a 6 kg mol^{-1} P2VP-OH brush. EDX elemental maps in Figure 6 (b) show the film with titanium and oxygen signals present. Figure S16 shows the film before UV/ozone and Figure S17 – S18 are of the process applied to the 4 kg

mol^{-1} P2VP-OH brush. A thinner TiO_2 film (≈ 2 nm) is fabricated using the 4 kg mol^{-1} brush showing that our process can be used to tune TiO_2 films with nanometer control. For comparison, the TTIP infiltration process was applied to the 6 kg mol^{-1} PS-OH grafted brush (Figure S19). PS-OH grafted brushes exhibit excellent potential for blocking TTIP infiltration with EDX maps confirming that the precursor is inhibited by the PS brush with no Ti present at the substrate interface. The process can be further optimized by using a higher molecular weight PS brush, tuning TTIP vapor pressure and exposure time.

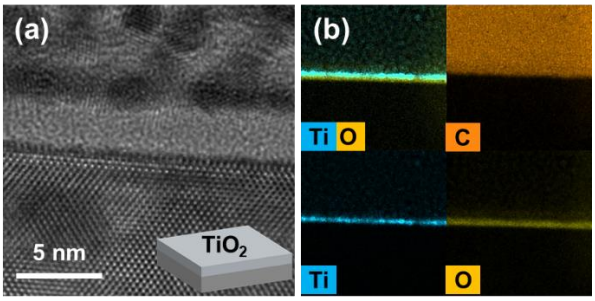

Figure 6. (a) Bright-field TEM image of the titanium dioxide film (after uv/ozone) and **(b)** the corresponding EDX maps (Ti, C, O) following TTIP treatment of a uniform P2VP-OH brush film (Mn = 6 kg mol^{-1}) .

CONCLUSIONS

High quality titania films were fabricated using simple apparatus that allowed definition of precise polymer films for hosting titanium precursors using a facile vapour phase infiltration technique. It was shown that very high coverage, pin hole free, homogeneous titania films could be produced of controlled thickness. This article discussed the precise parameters required for end-grafting monolayer P2VP-OH polymer brushes (polymer molecular weight, casting solution concentration and terminal group density). The brush layer deposition/attachment requires careful optimization to allow monolayer formation. This facilitates the regularity of the inorganic film. As the brushes contain active groups that bind metal, there is a propensity for coordination of the polymer to form aggregates in solution and 3D films that mitigate against precise monolayer formation. This work shows that process conditions and treatments can be created to mitigate these difficulties.

Brushes that contain metal binding sites can be used to fabricate high quality inorganic films. A vapor phase infiltration approach using a Ti precursor into monolayer brush films was demonstrated on grafted P2VP-OH. Grafting comparison of P2VP with PS and PMMA highlights the strong pyridine stacking interactions that inhibit film formation above the CAC. The results show that the initial polymer films need very careful tuning for uniform inorganic films. High-quality grafted P2VP-OH brushes were exposed to vapor phase TTIP and conversion to TiO_2 is performed using UV/ozone processing. Control over the final oxide thickness (≈ 2-4 nm) is demonstrated by adjusting the polymer molecular weight. P2VP is an ideal system for metal incorporation, however developing thicker films with PVP brushes is prohibitive due to strong intermolecular forces. Less reactive brushes such as PMMA may be more suitable for fabricating thick inorganic films and studies are underway. PS brushes have excellent promise for surface deactivation where TTIP deposition was completely prevented from reaching the substrate. In summary, we precisely controlled polymer brushes for activating (P2VP-OH) and deactivating (PS-OH) semiconductor surfaces, which is a critical milestone for fulfilling future device scaling and 3D architecture. Our deposition and brush process could also find use in other sectors that rely on uniform nanometer inorganic films e.g. glass coating technologies (self-cleaning, anti-condensation, low emissivity etc.), digital display (electrode, conductive and emissive LCD/LED/OLED layers).

ASSOCIATED CONTENT

Supporting Information. Grafting data for PS-OH and PMMA-OH. Additional XPS, EDX and electron microscopy data.
This material is available free of charge via the Internet at http://pubs.acs.org.

AUTHOR INFORMATION

Corresponding Authors

* E-mail: ross.lundy2@gmail.com (R.L.)
* E-mail: morrism2@tcd.ie (M.A.M.)

C.Cummins – Current affiliation:

Univ. Bordeaux, CNRS, Centre de Recherche Paul Pascal (CRPP), UMR 5031, 33600 Pessac, France.

Laboratoire de Chimie des Polymères Organiques (LCPO), CNRS UMR 5629, ENSCPB, Université de Bordeaux, 16 Avenue Pey-Berland, F-33607 Pessac Cedex, France

Author Contributions

‡R.L. and P.Y. contributed equally.

Notes

The authors declare no competing financial interest.

ACKNOWLEDGMENT

We gratefully acknowledge the work of Alan Bell, Chris O'Neill and David Bird in Intel Analytical Labs for providing technical assistance with TEM imaging and sample preparation. We thank Matt Shaw, Jennifer McKenna and Alan Bell (Intel) for technical advice and discussions. RL gratefully acknowledges the staff of the Advanced Microscopy Laboratory (AML), Trinity College Dublin for their assistance during characterization. This publication has emanated from research conducted with the financial support of Science Foundation Ireland (SFI) under grant number 12/RC/2278 and 16/SP/3809. This research is also co-funded by the European Regional Development Fund and Science Foundation Ireland under Ireland's European Structural and Investment Fund.

REFERENCES

(1) Morris, M. A. Directed Self-Assembly of Block Copolymers for Nanocircuitry Fabrication. *Microelectron. Eng.* **2015**, *132*, 207–217. https://doi.org/10.1016/j.mee.2014.08.009.

(2) Samsung Electronics' Leadership in Advanced Foundry Technology Showcased with Latest Silicon Innovations and Ecosystem Platform https://news.samsung.com/global/samsung-electronics-leadership-in-advanced-foundry-technology-showcased-with-latest-silicon-innovations-and-ecosystem-platform (accessed Dec 3, 2019).

(3) TSMC starts work on US$19.6 Billion 3nm fab i... | Taiwan News https://www.taiwannews.com.tw/en/news/3805032 (accessed Dec 3, 2019).

(4) Bae, G.; Bae, D. I.; Kang, M.; Hwang, S. M.; Kim, S. S.; Seo, B.; Kwon, T. Y.; Lee, T. J.; Moon, C.; Choi, Y. M.; et al. 3nm GAA Technology Featuring Multi-Bridge-Channel FET for Low Power and High Performance Applications. In *Technical Digest - International Electron Devices Meeting, IEDM*; Institute of Electrical and Electronics Engineers Inc., 2019; Vol. 2018-Decem, pp 28.7.1-28.7.4. https://doi.org/10.1109/IEDM.2018.8614629.

(5) Mårtensson, T.; Carlberg, P.; Borgström, M.; Montelius, L.; Seifert, W.; Samuelson, L. Nanowire Arrays Defined by Nanoimprint Lithography. *Nano Lett.* **2004**, *4* (4), 699–702. https://doi.org/10.1021/nl035100s.

(6) Borah, D.; Cummins, C.; Rasappa, S.; Senthamaraikannan, R.; Salaun, M.; Zelsmann, M.; Liontos, G.; Ntetsikas, K.; Avgeropoulos, A.; Morris, M.; et al. Nanopatterning via Self-Assembly of a Lamellar-Forming Polystyrene-Block-Poly(Dimethylsiloxane) Diblock Copolymer on Topographical Substrates Fabricated by Nanoimprint Lithography. *Nanomaterials* **2018**, *8* (1), 32. https://doi.org/10.3390/nano8010032.

(7) Cummins, C.; Mokarian-Tabari, P.; Andreazza, P.; Sinturel, C.; Morris, M. A. Solvothermal Vapor Annealing of Lamellar Poly(Styrene)-Block-Poly(d,l-Lactide) Block Copolymer Thin Films for Directed Self-Assembly Application. *ACS Appl. Mater. Interfaces* **2016**. https://doi.org/10.1021/acsami.6b00765.

(8) Ross, C. a; Berggren, K. K.; Cheng, J. Y.; Jung, Y. S.; Chang, J.-B. Three-Dimensional Nanofabrication by Block Copolymer Self-Assembly. *Adv. Mater.* **2014**, *26* (25), 4386–4396. https://doi.org/10.1002/adma.201400386.

(9) Oh, J.; Suh, H. S.; Ko, Y.; Nah, Y.; Lee, J.-C.; Yeom, B.; Char, K.; Ross, C. A.; Son, J. G. Universal Perpendicular Orientation of Block Copolymer Microdomains Using a Filtered Plasma. *Nat. Commun.* **2019**, *10* (1), 2912. https://doi.org/10.1038/s41467-019-10907-5.

(10) Fernandez, E.; Tu, K. H.; Ho, P.; Ross, C. A. Thermal Stability of L10-FePt Nanodots Patterned by Self-Assembled Block Copolymer Lithography. *Nanotechnology* **2018**, *29* (46), 465301. https://doi.org/10.1088/1361-6528/aade2f.

(11) Tu, K.-H.; Bai, W.; Liontos, G.; Ntetsikas, K.; Avgeropoulos, A.; Ross, C. a. Universal Pattern Transfer Methods for Metal Nanostructures by Block Copolymer Lithography. *Nanotechnology* **2015**, *26* (37), 375301. https://doi.org/10.1088/0957-4484/26/37/375301.

(12) Gotrik, K. W.; Hannon, A. F.; Son, J. G.; Keller, B.; Alexander-katz, A.; Ross, C. A. Morphology Control in Block Copolymer Films Using Mixed Solvent Vapors, 2012.

(13) Lundy, R.; Flynn, S. P.; Cummins, C.; Kelleher, S. M.; Collins, M. N.; Dalton, E.; Daniels, S.; Morris, M. A.; Enright, R. Controlled Solvent Vapor Annealing of a High χ Block Copolymer Thin Film. *Phys. Chem. Chem. Phys.* **2017**, *19* (4), 2805–2815. https://doi.org/10.1039/C6CP07633E.

(14) Lundy, R.; Flynn, S. P.; Cummins, C.; Kelleher, S. M.; Collins, M. N.; Dalton, E.; Daniels, S.; Morris, M.; Enright, R. Nanoporous Membrane Production via Block Copolymer Lithography for High Heat Dissipation Systems. In *2016 15th IEEE Intersociety Conference on Thermal and Thermomechanical Phenomena in Electronic Systems (ITherm)*; IEEE, 2016; pp 1267–1272.

(15) Mackus, A. J. M.; Merkx, M. J. M.; Kessels, W. M. M. From the Bottom-Up: Toward Area-Selective Atomic Layer Deposition with High Selectivity †. *Chem. Mater.* **2019**, *31* (1), 2–12. https://doi.org/10.1021/acs.chemmater.8b03454.

(16) Seo, S.; Yeo, B. C.; Han, S. S.; Yoon, C. M.; Yang, J. Y.; Yoon, J.; Yoo, C.; Kim, H. J.; Lee, Y. B.; Lee, S. J.; et al. Reaction Mechanism of Area-Selective Atomic Layer Deposition for Al2O3 Nanopatterns. *ACS Appl. Mater. Interfaces* **2017**, *9* (47), 41607–41617. https://doi.org/10.1021/acsami.7b13365.

(17) Prasittichai, C.; Pickrahn, K. L.; Minaye Hashemi, F. S.; Bergsman, D. S.; Bent, S. F. Improving Area-Selective Molecular Layer Deposition by Selective SAM Removal. *ACS Appl. Mater. Interfaces* **2014**, *6* (20), 17831–17836. https://doi.org/10.1021/am504441e.

(18) Nagata, T. *Material Design of Metal/Oxide Interfaces for Nanoelectronics Applications*, 1st ed.; Springer Japan, 2020.

(19) IEEE International Interconnect Technology Conference/Advanced Metallization Conference (IITC/AMC); 2016; pp 133–135.

(20) Li, R.; Zhang, F.; Wang, D.; Yang, J.; Li, M.; Zhu, J.; Zhou, X.; Han, H.; Li, C. Spatial Separation of Photogenerated Electrons and Holes among {010} and {110} Crystal Facets of BiVO 4. *Nat. Commun.* **2013**, *4*. https://doi.org/10.1038/ncomms2401.

(21) Xie, J.; Yang, X.; Han, B.; Shao-Horn, Y.; Wang, D. Site-Selective Deposition of Twinned Platinum Nanoparticles on TiSi 2 Nanonets by Atomic Layer Deposition and Their Oxygen Reduction Activities. *ACS Nano* **2013**, *7* (7), 6337–6345. https://doi.org/10.1021/nn402385f.

(22) Jiang, X.; Huang, H.; Prinz, F. B.; Bent, S. F. Application of Atomic Layer Deposite of Platinum to Solid Oxide Fuel Cells. *Chem. Mater.* **2008**, *20* (12), 3897–3905. https://doi.org/10.1021/cm7033189.

(23) Färm, E.; Kemell, M.; Ritala, M.; Leskelä, M. Self-Assembled Octadecyltrimethoxysilane Monolayers Enabling Selective-Area Atomic Layer Deposition of Iridium. *Chem. Vap. Depos.* **2006**, *12* (7), 415–417. https://doi.org/10.1002/cvde.200604219.

(24) Färm, E.; Kemell, M.; Ritala, M.; Leskelä, M. Selective-Area Atomic Layer Deposition with Microcontact Printed Self-Assembled Octadecyltrichlorosilane Monolayers as Mask Layers. *Thin Solid Films* **2008**, *517* (2), 972–975. https://doi.org/10.1016/J.TSF.2008.08.191.

(25) Färm, E.; Vehkamäki, M.; Ritala, M.; Leskelä, M. Passivation of Copper Surfaces for Selective-Area ALD Using a Thiol Self-Assembled Monolayer. *Semicond. Sci. Technol.* **2012**, *27* (7), 074004. https://doi.org/10.1088/0268-1242/27/7/074004.

(26) Färm, E.; Lindroos, S.; Ritala, M.; Markku, L. Microcontact Printed Films as an Activation Layer for Selective Atomic Layer Deposition, July 8, 2011.

(27) Färm, E.; Lindroos, S.; Ritala, M.; Leskelä, M. Microcontact Printed RuO x Film as an Activation Layer for Selective-Area Atomic Layer Deposition of Ruthenium. *Chem. Mater.* **2012**, *24* (2), 275–278. https://doi.org/10.1021/cm202468s.

(28) Färm, E.; Kemell, M.; Ritala, M.; Leskelä, M. Selective-Area Atomic Layer Deposition Using Poly(Methyl Methacrylate) Films as Mask Layers. *J. Phys. Chem. C* **2008**, *112* (40), 15791–15795. https://doi.org/10.1021/jp803872s.

(29) Färm, E.; Kemell, M.; Santala, E.; Ritala, M.; Leskelä, M. Selective-Area Atomic Layer Deposition Using Poly(Vinyl Pyrrolidone) as a Passivation Layer. *J. Electrochem. Soc.* **2010**, *157* (1), K10. https://doi.org/10.1149/1.3250936.

(30) Minaye Hashemi, F. S.; Prasittichai, C.; Bent, S. F. Self-Correcting Process for High Quality Patterning by Atomic Layer Deposition. *ACS Nano* **2015**, *9* (9), 8710–8717. https://doi.org/10.1021/acsnano.5b03125.

(31) Minaye Hashemi, F. S.; Birchansky, B. R.; Bent, S. F. Selective Deposition of Dielectrics: Limits and Advantages of Alkanethiol Blocking Agents on Metal-Dielectric Patterns. *ACS Appl. Mater. Interfaces* **2016**, *8* (48), 33264–33272. https://doi.org/10.1021/acsami.6b09960.

(32) Chen, R.; Kim, H.; McIntyre, P. C.; Bent, S. F. Self-Assembled Monolayer Resist for Atomic Layer Deposition of HfO2 and ZrO2 High-κ Gate Dielectrics. *Appl. Phys. Lett.* **2004**, *84* (20), 4017–4019. https://doi.org/10.1063/1.1751211.

(33) Chen, R.; Kim, H.; McIntyre, P. C.; Bent, S. F. Investigation of Self-Assembled Monolayer Resists for Hafnium Dioxide Atomic Layer Deposition. *Chem. Mater.* **2005**, *17* (3), 536–544. https://doi.org/10.1021/cm0486666.

(34) Junsic, H.; Porter, D. W.; Sreenivasan, R.; McIntyre, P. C.; Bent, S. F. ALD Resist Formed by Vapor-Deposited Self-Assembled Monolayers. *Langmuir* **2007**, *23* (3), 1160–1165. https://doi.org/10.1021/la0606401.

(35) Jiang, X.; Bent, S. F. Area-Selective ALD with Soft Lithographic Methods: Using Self-Assembled Monolayers to Direct Film Deposition. *J. Phys. Chem. C* **2009**, *113* (41), 17613–17625. https://doi.org/10.1021/jp905317n.

(36) Bobb-Semple, D.; Nardi, K. L.; Draeger, N.; Hausmann, D. M.; Bent, S. F. Area-Selective Atomic Layer Deposition Assisted by Self-Assembled Monolayers: A Comparison of Cu, Co, W, and Ru. *Chem. Mater.* **2019**, *31* (5), 1635–1645. https://doi.org/10.1021/acs.chemmater.8b04926.

(37) Kim, W. H.; Minaye Hashemi, F. S.; Mackus, A. J. M.; Singh, J.; Kim, Y.; Bobb-Semple, D.; Fan, Y.; Kaufman-Osborn, T.; Godet, L.; Bent, S. F. A Process for Topographically Selective Deposition on 3D Nanostructures by Ion Implantation. *ACS Nano* **2016**, *10* (4), 4451–4458. https://doi.org/10.1021/acsnano.6b00094.

(38) Vervuurt, R. H. J.; Sharma, A.; Jiao, Y.; Kessels, W. (Erwin) M. M.; Bol, A. A. Area-Selective Atomic Layer Deposition of Platinum Using Photosensitive Polyimide. *Nanotechnology* **2016**, *27* (40), 405302. https://doi.org/10.1088/0957-4484/27/40/405302.

(39) Mameli, A.; Kuang, Y.; Aghaee, M.; Ande, C. K.; Karasulu, B.; Creatore, M.; Mackus, A. J. M.; Kessels, W. M. M.; Roozeboom, F. Area-Selective Atomic Layer Deposition of In_2O_3:H Using a μ-Plasma Printer for Local Area Activation. *Chem. Mater.* **2017**, *29* (3), 921–925. https://doi.org/10.1021/acs.chemmater.6b04469.

(40) MacKus, A. J. M.; Verheijen, M. A.; Leick, N.; Bol, A. A.; Kessels, W. M. M. Influence of Oxygen Exposure on the Nucleation of Platinum Atomic Layer Deposition: Consequences for Film Growth, Nanopatterning, and Nanoparticle Synthesis. *Chem. Mater.* **2013**, *25* (9), 1905–1911. https://doi.org/10.1021/cm400562u.

(41) Thissen, N. F. W.; Vervuurt, R. H. J.; Mackus, A. J. M.; Mulders, J. J. L.; Weber, J.-W.; Kessels, W. M. M.; Bol, A. A. Graphene Devices with Bottom-up Contacts by Area-Selective Atomic Layer Deposition. *2D Mater.* **2017**, *4* (2), 025046. https://doi.org/10.1088/2053-1583/aa636a.

(42) Mameli, A.; Karasulu, B.; Verheijen, M. A.; Barcones, B.; Macco, B.; Mackus, A. J. M.; Kessels, W. M. M. E.; Roozeboom, F. Area-Selective Atomic Layer Deposition of ZnO by Area Activation Using Electron Beam-Induced Deposition. *Chem. Mater.* **2019**, *31* (4), 1250–1257. https://doi.org/10.1021/acs.chemmater.8b03165.

(43) Singh, J. A.; Thissen, N. F. W.; Kim, W.-H.; Johnson, H.; Kessels, W. M. M.; Bol, A. A.; Bent, S. F.; Mackus, A. J. M. Area-Selective Atomic Layer Deposition of Metal Oxides on Noble Metals through Catalytic Oxygen Activation. *Chem. Mater.* **2018**, *30* (3), 663–670. https://doi.org/10.1021/acs.chemmater.7b03818.

(44) Mameli, A.; Merkx, M. J. M.; Karasulu, B.; Roozeboom, F.; Kessels, W. (Erwin) M. M.; Mackus, A. J. M. Area-Selective Atomic Layer Deposition of SiO_2 Using Acetylacetone as a Chemoselective Inhibitor in an ABC-Type Cycle. *ACS Nano* **2017**, *11* (9), 9303–9311. https://doi.org/10.1021/acsnano.7b04701.

(45) Vos, M. F. J.; Chopra, S. N.; Verheijen, M. A.; Ekerdt, J. G.; Agarwal, S.; Kessels, W. M. M.; Mackus, A. J. M. Area-Selective Deposition of Ruthenium by Combining Atomic Layer Deposition and Selective Etching. *Chem. Mater.* **2019**, *31* (11), 3878–3882. https://doi.org/10.1021/acs.chemmater.9b00193.

(46) Park, K. J.; Doub, J. M.; Gougousi, T.; Parsons, G. N. Microcontact Patterning of Ruthenium Gate Electrodes by Selective Area Atomic Layer Deposition. *Appl. Phys. Lett.* **2005**, *86* (5), 051903. https://doi.org/10.1063/1.1852079.

(47) Stevens, E.; Tomczak, Y.; Chan, B. T.; Altamirano Sanchez, E.; Parsons, G. N.; Delabie, A. Area-Selective Atomic Layer Deposition of TiN, TiO_2, and HfO_2 on Silicon Nitride with Inhibition on Amorphous Carbon. *Chem. Mater.* **2018**, *30* (10), 3223–3232. https://doi.org/10.1021/acs.chemmater.8b00017.

(48) Atanasov, S. E.; Kalanyan, B.; Parsons, G. N. Inherent Substrate-Dependent Growth Initiation and Selective-Area Atomic Layer Deposition of TiO_2 Using "Water-Free" Metal-Halide/Metal Alkoxide Reactants. *J. Vac. Sci. Technol. A Vacuum, Surfaces, Film.* **2016**, *34* (1), 01A148. https://doi.org/10.1116/1.4938481.

(49) Parsons, G. N.; Kalanyan, B.; Atanasov, S. E.; Lemaire, P.; Oldham, C. (Invited) Using Inherent Substrate-Dependent Nucleation to Promote Metal and Metal Oxide Selective-Area Atomic Layer Deposition. *ECS Trans.* **2016**, *75* (6), 77–83. https://doi.org/10.1149/07506.0077ecst.

(50) Parsons, G. N. Functional Model for Analysis of ALD Nucleation and Quantification of Area-Selective Deposition. *J. Vac. Sci. Technol. A* **2019**, *37* (2), 020911. https://doi.org/10.1116/1.5054285.

(51) SONG, S. K.; Saare, H.; Parsons, G. N. Integrated Isothermal Atomic Layer Deposition/Atomic Layer Etching Super-Cycles for Area-Selective Deposition of TiO_2. *Chem. Mater.* **2019**, acs.chemmater.9b01143. https://doi.org/10.1021/acs.chemmater.9b01143.

(52) Zhang, Y.; Discekici, E. H.; Burns, R. L.; Somervell, M.; Hawker, C. J.; Bates, C. M. A Single-Step, Spin-on Process for High Fidelity and Selective Polymer Deposition. *ACS Appl. Polym. Mater.* **2019**, acsapm.9b00914. https://doi.org/10.1021/acsapm.9b00914.

(53) Zhang, Y.; D'Ambra, C. A.; Katsumata, R.; Burns, R. L.; Somervell, M. H.; Segalman, R. A.; Hawker, C. J.; Bates, C. M. Rapid and Selective Deposition of Patterned Thin Films on Heterogeneous Substrates via Spin Coating. *ACS Appl. Mater. Interfaces* **2019**, *11* (23), 21177–21183. https://doi.org/10.1021/acsami.9b05190.

(54) Cummins, C.; Weingärtner, T.; Morris, M. A. Enabling Large-Area Selective Deposition on Metal-Dielectric Patterns Using Polymer Brush Deactivation. *J. Phys. Chem. C* **2018**, *122* (26), 14698–14705. https://doi.org/10.1021/acs.jpcc.8b04092.

(55) Lundy, R.; Yadav, P.; Selkirk, A.; Mullen, E.; Ghoshal, T.; Cummins, C.; Morris, M. A. Optimizing Polymer Brush Coverage To Develop Highly Coherent Sub-5 Nm Oxide Films by Ion Inclusion. *Chem. Mater.* **2019**, *31* (22), 9338–9345. https://doi.org/10.1021/acs.chemmater.9b02856.

(56) Cummins, C.; Shaw, M. T.; Morris, M. A. Area Selective Polymer Brush Deposition. *Macromol. Rapid Commun.* **2017**, *38* (16), 1700252. https://doi.org/10.1002/marc.201700252.

(57) Snelgrove, M.; Mani-Gonzalez, P. G.; Bogan, J.; Lundy, R.; Rueff, J. P.; Hughes, G.; Yadav, P.; McGlynn, E.; Morris, M.; O'Connor, R. Hard X-Ray Photoelectron Spectroscopy Study of Copper Formation by Metal Salt Inclusion in a Polymer Film. *J. Phys. D. Appl. Phys.* **2019**, *52* (43). https://doi.org/10.1088/1361-6463/ab35b2.

(58) Mani-Gonzalez, P. G.; Snelgrove, M.; Rueff, J.-P.; Lundy, R.; Yadav, P.; Bogan, J.; O'Connor, R.; Morris, M.; Hughes, G. Analysis of Al and Cu Salt Infiltration into a Poly 2-Vinylpyridine (P2vP) Polymer Layer for Semiconductor Device Patterning Applications. *J. Phys. D. Appl. Phys.* **2019**, 1–20. https://doi.org/10.1088/1361-6463/ab60e8.

(59) Walia, S. *Low Power Semiconductor Devices and Processes for Emerging Applications in Communications, Computing, and Sensing*; CRC Press, 2018. https://doi.org/10.1201/9780429503634.

(60) Wang, C. C.; Ying, J. Y. Sol-Gel Synthesis and Hydrothermal Processing of Anatase and Rutile Titania Nanocrystals. *Chem. Mater.* **1999**, *11* (11), 3113–3120. https://doi.org/10.1021/cm990180f.

(61) Major, B.; Ebner, R.; Zięba, P.; Wolczyński, W. Titanium-Based Films Deposited Using a Nd:YAG Pulsed Laser. *Appl. Phys. A Mater. Sci. Process.* **1999**, *69* (7). https://doi.org/10.1007/s003390051559.

(62) Shi, J.; Wang, X. Growth of Rutile Titanium Dioxide Nanowires by Pulsed Chemical Vapor Deposition. *Cryst. Growth Des.* **2011**, *11* (4), 949–954. https://doi.org/10.1021/cg200140k.

(63) Klesko, J. P.; Rahman, R.; Dangerfield, A.; Nanayakkara, C. E.; L'Esperance, T.; Moser, D. F.; Fabián Peña, L.; Mattson, E. C.; Dezelah, C. L.; Kanjolia, R. K.; et al. Selective Atomic Layer Deposition Mechanism for Titanium Dioxide Films with (EtCp)Ti(NMe2)3: Ozone versus Water. *Chem. Mater.* **2018**, *30* (3), 970–981. https://doi.org/10.1021/acs.chemmater.7b04790.

(64) Ritala, M.; Leskela, M.; Niinisto, L.; Haussalo, P. Titanium Isopropoxide as a Precursor in Atomic Layer Epitaxy of Titanium Dioxide Thin Films. *Chem. Mater.* **1993**, *5* (8), 1174–1181. https://doi.org/10.1021/cm00032a023.

(65) Ganesh, V. A.; Raut, H. K.; Nair, A. S.; Ramakrishna, S. A Review on Self-Cleaning Coatings. *Journal of Materials Chemistry*. November 7, 2011, pp 16304–16322. https://doi.org/10.1039/c1jm12523k.

(66) Usai, S.; Walsh, J. J. Facile Assembly of Polyoxometalate-Polyelectrolyte Films on Nano-MO2(M = Sn, Ti) for Optical Applications. *J. Electroanal. Chem.* **2018**, *815* (March), 86–89. https://doi.org/10.1016/j.jelechem.2018.03.007.

(67) Busani, T.; Devine, R. A. B. Dielectric and Infrared Properties of TiO $_2$ Films Containing Anatase and Rutile. *Semicond. Sci. Technol.* **2005**, *20* (8), 870–875. https://doi.org/10.1088/0268-1242/20/8/043.

(68) Rahimi, N.; Pax, R. A.; Gray, E. M. A. Review of Functional Titanium Oxides. I: TiO2and Its Modifications. *Prog. Solid State Chem.* **2016**, *44* (3), 86–105. https://doi.org/10.1016/j.progsolidstchem.2016.07.002.

(69) Daubert, J. S.; Hill, G. T.; Gotsch, H. N.; Gremaud, A. P.; Ovental, J. S.; Williams, P. S.; Oldham, C. J.; Parsons, G. N. Corrosion Protection of Copper Using Al $_2$ O $_3$, TiO $_2$, ZnO, HfO $_2$, and ZrO $_2$ Atomic Layer Deposition. *ACS Appl. Mater. Interfaces* **2017**, *9* (4), 4192–4201. https://doi.org/10.1021/acsami.6b13571.

(70) Zardetto, V.; Williams, B. L.; Perrotta, A.; Di Giacomo, F.; Verheijen, M. A.; Andriessen, R.; Kessels, W. M. M.; Creatore, M. Atomic Layer Deposition for Perovskite Solar Cells: Research Status, Opportunities and Challenges. *Sustainable Energy and Fuels*. Royal Society of Chemistry 2017, pp 30–55. https://doi.org/10.1039/c6se00076b.

(71) Liao, S. Y.; Yang, Y. C.; Huang, S. H.; Gan, J. Y. Synthesis of Pt@TiO2@CNTs Hierarchical Structure Catalyst by Atomic Layer Deposition and Their Photocatalytic and Photoelectrochemical Activity. *Nanomaterials* **2017**, *7* (5). https://doi.org/10.3390/nano7050097.

(72) Kulmas, M.; Paterson, L.; Höflich, K.; Bashouti, M. Y.; Wu, Y.; Göbelt, M.; Ristein, J.; Bachmann, J.; Meyer, B.; Christiansen, S. Composite Nanostructures of TiO $_2$ and ZnO for Water Splitting Application: Atomic Layer Deposition Growth and Density Functional Theory Investigation. *Adv. Funct. Mater.* **2016**, *26* (27), 4882–4889. https://doi.org/10.1002/adfm.201505524.

(73) Rodgers, M. T.; Stanley, J. R.; Amunugama, R. Periodic Trends in the Binding of Metal Ions to Pyridine Studied by Threshold Collision-Induced Dissociation and Density Functional Theory. *J. Am. Chem. Soc.* **2000**, *122* (44), 10969–10978. https://doi.org/10.1021/ja0027923.

(74) Kennemur, J. G. Poly(Vinylpyridine) Segments in Block Copolymers: Synthesis, Self-Assembly, and Versatility. *Macromolecules* **2019**, *52* (4), 1354–1370. https://doi.org/10.1021/acs.macromol.8b01661.

(75) Giraud, E. C.; Mokarian-Tabari, P.; Toolan, D. T. W.; Arnold, T.; Smith, A. J.; Howse, J. R.; Topham, P. D.; Morris, M. A. Highly Ordered Titanium Dioxide Nanostructures via a Simple One-Step Vapor-Inclusion Method in Block Copolymer Films. *ACS Appl. Nano Mater.* **2018**, *1* (7), 3426–3434. https://doi.org/10.1021/acsanm.8b00632.

(76) Brinker, C. J. Hydrolysis and Condensation of Silicates: Effects on Structure. *J. Non. Cryst. Solids* **1988**, *100* (1–3), 31–50. https://doi.org/10.1016/0022-3093(88)90005-1.

(77) Lebrun, J. J.; Porte, H. Polysiloxanes. *Compr. Polym. Sci. Suppl.* **1989**, 593–609. https://doi.org/10.1016/B978-0-08-096701-1.00175-0.

(78) Siefering, K. L.; Griffin, G. L. Growth Kinetics of CVD TiO2: Influence of Carrier Gas. *J. Electrochem. Soc.* **1990**, *137* (4), 1206–1208. https://doi.org/10.1149/1.2086632.

(79) Ma, K.-X.; Ho, C.-H.; Zhu, F.; Chung, T.-S. Investigation of Surface Energy for Organic Light Emitting Polymers and Indium Tin Oxide. *Thin Solid Films* **2000**, *371* (1–2), 140–147. https://doi.org/10.1016/S0040-6090(00)00994-9.

(80) Sierański, T. Discovering the Stacking Landscape of a Pyridine-Pyridine System. *J. Mol. Model.* **2017**, *23* (12), 338. https://doi.org/10.1007/s00894-017-3496-4.

(81) Cassie, A. B. D.; Baxter, S. Wettability of Porous Surfaces. *Trans. Faraday Soc.* **1944**, *40*, 546–551.

(82) Lundy, R.; Byrne, C.; Bogan, J.; Nolan, K.; Collins, M. N.; Dalton, E.; Enright, R. Exploring the Role of Adsorption and Surface State on the Hydrophobicity of Rare Earth Oxides. *ACS Appl. Mater. Interfaces* **2017**. https://doi.org/10.1021/acsami.7b01515.

(83) Laibinis, P. E.; Whitesides, G. M. ..Omega.-Terminated Alkanethiolate Monolayers on Surfaces of Copper, Silver, and Gold Have Similar Wettabilities. *J. Am. Chem. Soc.* **1992**, *114* (6), 1990–1995. https://doi.org/10.1021/ja00032a009.

(84) Wenzel, R. Resistance of Solid Surfaces to Wetting by Water. *Ind. Eng. Chem.* **1936**, *28* (8), 988–994.

(85) Liu, F. M.; Wang, T. M. Surface and Optical Properties of Nanocrystalline Anatase Titania Films Grown by Radio Frequency Reactive Magnetron Sputtering. *Appl. Surf. Sci.* **2002**, *195* (1–4), 284–290. https://doi.org/10.1016/S0169-4332(02)00569-X.

(86) Snelgrove, M.; Zehe, C.; Lundy, R.; Yadav, P.; Rueff, J.-P.; O'Connor, R.; Bogan, J.; Hughes, G.; McGlynn, E.; Morris, M.; et al. Surface Characterization of Poly-2-Vinylpyridine—A Polymer for Area Selective Deposition Techniques. *J. Vac. Sci. Technol. A* **2019**, *37* (5), 050601. https://doi.org/10.1116/1.5115769.

(87) Si, W.; Lei, W.; Hao, Q.; Xia, X.; Zhang, H.; Li, J.; Li, Q.; Cong, R. Facile Synthesis of Nitrogen-Doped Graphene Derived from Graphene Oxide and Vitamin B3 as High-Performance Sensor for Imidacloprid Determination. *Electrochim. Acta* **2016**, *212*, 784–790. https://doi.org/10.1016/j.electacta.2016.07.063.

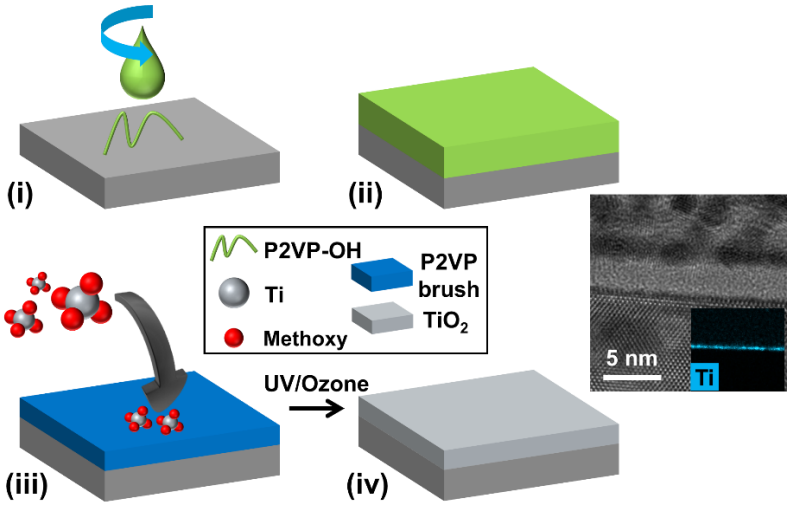

TOC Image